

The Fornax Deep Survey with VST: presentation of the spectroscopic survey and compilation of the globular cluster catalogue

Vincenzo Pota et al. ^{1*},

¹ INAF – Osservatorio Astronomico di Capodimonte, Salita Moiariello, 16, 80131 - Napoli, Italy

10 February 2018

ABSTRACT

We present the results of a large spectroscopic survey aimed at detecting extragalactic globular clusters (GCs) in the core of the Fornax cluster, as part of the Fornax Deep Survey. GC candidates were selected in multi-band VST and VISTA images. About 4500 low resolution spectra (from 4800 to 10000Å) were observed in 25 VLT/VIMOS masks covering the central 1 deg² around the dominant galaxy NGC 1399. We describe the methodology used for data reduction and data analysis. We found a total of 387 unique physical objects (372 GCs and 15 ultra compact dwarfs) associated to galaxies in the sampled field. Most of these objects are associated to NGC 1399, with only 10% likely associated to other giant galaxies. This new dataset is complementary to the many GC catalogues already present in the literature and it brings the total number of trace particles around NGC 1399 to over a thousand. This is a valuable reference for the study of the galaxy cluster environment and for the dynamics and kinematics of giant galaxies.

Key words: galaxies:star clusters – galaxies:evolution– galaxies: kinematics and dynamics

1 INTRODUCTION

Nearby galaxy clusters are ideal laboratories for studying the evolution of low- and high mass galaxies as well as dense stellar systems (globular clusters, compact dwarf galaxies, etc.) in dense environments. The Virgo and Fornax clusters are closest galaxy clusters, hence provide a unique laboratory to test galaxy formation theories.

The Fornax Deep Survey¹ (FDS) aims to study the formation and assembly of the Fornax Cluster out to its viral radius with a variety of observations. These include deep photometry, multi-object and wide-field spectroscopy, supplemented by cross-match with other wavelength observations such as X-rays (e.g. Paolillo et al. 2002). The cornerstone of FDS is deep multiband (*u*, *g*, *r* and *i*) imaging data from the VST/OmegaCam camera covering an area of ~ 30 deg² of the cluster out the viral radius. The area also includes the Fornax-A subgroups, hence providing a full coverage of the cluster structure under assembly. The depth of the imaging dataset reaches ~ 30 mag/arcsec² in the *g*-band (see Iodice et al. 2016, 2017), among the deepest acquired on the cluster so far (Venhola et al. 2018). VISTA/VIRCAM observations in J and K (K_s = 23.4 AB mag, and J = 23.4 AB mag) are also available (see e.g. Munoz et

al. 2015), to complement the optical data and optimise galaxy and globular cluster membership and the selection of follow-up targets (e.g. globular clusters, GCs hereafter, and/or Ultra Compact Dwarf galaxies, UCDs hereafter).

The multi-band deep images have been used to study the light distribution and colors of cluster galaxies out to 8-10 effective radii and beyond to characterise the faint galaxy haloes and have revealed the presence of ultra-faint stellar structures in the core of Fornax: fingerprints of past and ongoing interaction between galaxies falling into the deep potential well of the cluster (Iodice et al. 2016, Venhola et al. 2017). The same conclusion is backed-up by the complex distribution of globular clusters in the Fornax cluster (DAbrusco et al. 2016, Cantiello et al. 2017).

The Fornax cluster is the most massive galaxy structure after the Virgo cluster within 20 Mpc and it is an ideal target to study the effect of the environment on the structure and assembly of galaxies of any type, from the massive central giant early-type systems to the dwarf galaxies. Despite its regular appearance, it has been found that the assembly of the Fornax cluster is still ongoing. Although its core seems in an evolved phase (Grillmair et al. 1994; Jord an et al. 2007) and most of the bright ($m_B < 15$ mag) cluster members are early-type galaxies (Ferguson 1989), the presence of stellar and GC tidal streams (e.g. Iodice et al. 2016, DAbusco et al. 2016, Eisenhardt et al. 2017) have revealed that there are still signs of active galaxy interactions in the region inside 200 kpc, which mirrors the

* E-mail: vincenzo.pota@gmail.com

¹ ESO programme ID (094.B-0687)

large scale activity, including the accretion of the Fornax-A (NGC 1316) subgroup into the cluster core along a cosmic web filament (Drinkwater et al. 2001; Scharf et al. 2005).

To kinematically map the complexity of the cluster core out to at least 200 kpc using discrete kinematical tracers (e.g. GCs and UCDs) and finally connect the large scale kinematics down to the scale of the dwarf galaxies, we have started a number of spectroscopic follow-ups, which include integral field spectroscopy of dwarf galaxies with MUSE (see Mentz et al. 2016), and the multi-object spectroscopy of GC and UCDs candidates with VIMOS/VLT.

The ongoing FDS survey is a joint project based on Guaranteed Time Observation surveys, FOCUS (P.I. R. Peletier) and VEGAS (P.I. E. Iodice, Capaccioli et al. 2015). The radial velocity catalogue of GCs in Fornax presented in this paper is complementary to archival spectroscopic GC datasets of the Fornax cluster: Schuberth et al. (2010a) (which incorporates the catalogue of Dirsch et al. 2004), Bergond et al. (2007) and other catalogues discussed throughout the text. The assumed distance is 19.95 Mpc (Tonry et al. 2010).

The paper is structured as follows: Section 2 describes the data acquisition and reduction. The redshift estimation is discussed in Section 3, results are presented in Section 4 and discussed in 5. We summarise the results of the paper and conclude in Section 6.

2 DATA

This Section discusses all the steps undertaken to compile the spectroscopic catalogue discussed in this paper. The workflow consists in selecting a sample of GC candidates based on photometric selection criteria (§2.1) and use such a sample to design multi-object masks (§2.2) for follow-up observations (§2.3).

2.1 Selection of globular cluster candidates

The selection of GC candidates was based on VST/OmegaCAM photometry in the g and i band from the FDS survey (D'Abrusco et al. 2016; Iodice et al. 2016) and preliminary VISTA/VIRCAM photometry in the K_s band from the NGFS (Next Generation Fornax Survey, Muñoz et al. 2014). In the combined 2-colour giK_s diagram, confirmed GCs from Schuberth et al. (2010a) are confined to a restricted colour-colour space. We defined a polygon around the radial velocity members, which serves as prime selection criterion for our GC candidates. Of the 4340 unique spectroscopic targets (see Sect. 2.2) 4321 have giK_s photometry, and 2643 (or $\sim 61\%$) of those are confined in the selection polygon. We also applied a magnitude restriction of $17.0 < i < 23.0$ mag to our GC candidate sample in order to avoid a severe contamination by foreground stars on the bright side and too low signal-to-noise spectra on the faint side.

As an additional criterion we used the published wide-field Washington photometry from Dirsch et al. (2004) and Bassino et al. (2006) to construct a $C - i$ vs. $i - K_s$ diagram. Since the Washington C -band is similar to a u -band filter and the uiK_s plane is a very powerful tool to discriminate GCs from foreground and background objects (Muñoz et al. 2014), the CiK_s plane is the cleanest selection criterion. Unfortunately, the spatial coverage of the Washington photometry is not complete in the central square degree due to chip gaps and the restricted field-of-view. Out of the 1065 unique spectroscopic targets with CiK_s photometry, 809 (or $\sim 76\%$) are within this selection polygon.

Finally, for the very central regions of NGC 1399 which are dominated by the galaxy light, we added additional GC candidates based on the more accurate photometry and morphology derived from HST/ACS photometry by Puzia et al. (2014).

The FDS gi , the NGFS K_s , Washington C as well as the central ACS photometric catalogs were matched with SExtractor photometry of point and extended sources in all pre-images (ESO programme 094.B-0687(A)), which were taken in R -band prior to the spectroscopic observations. The x and y coordinates of sources in the pre-images are needed to create VIMOS catalogs for the creation of mask files with the VMMPS (VIMOS Mask Preparation Software,?) from ESO.

2.2 VIMOS pointings and mask design

A total of 25 VIMOS masks were designed covering the central square degree around NGC 1399. The masks were interleaved in such a way that the gaps between the four VIMOS CCDs (or quadrants) were covered by the adjacent mask.

In Figure 1 we show the spatial distribution of the VIMOS pointings, along with the footprints of archival observations in the same sky region from Schuberth et al. (2010a) and Bergond et al. (2007). It is clear that the mask distribution is much more homogeneous with respect to previous studies, although our target sampling varies across the field. The total covered area also contains other giant galaxies, namely, NGC 1404, NGC 1387 and NGC 1380. Figure 2 shows how the 2-dimensional density of allocated slits is considerably higher in the center with respect to the outskirts. Eight of the 25 pointings were dedicated to the central 25×25 arcmin to account for the higher density of GC candidates close to NGC 1399.

The use of the MR grism allows a multiplexing of two in wavelength direction (parallel to declination), i.e. spectra are not overlapping if slits are placed close to the bottom and top of the chip areas in all quadrants. For a first automatic slit allocation we used VMMPS with a catalog of GC candidates from the giK_s selection as input. Since the result of the automatic slit allocation was not satisfactory, we optimized the slit allocation of targets manually, for example by de-centering some targets in the slits while still keeping enough sky, or by allowing some overlap in wavelength range for multiplexed spectra, and by giving preference to targets that also fulfill the CiK_s selection criterion. The remaining free area on the chips was then filled with slits centered on GC candidates from the $(g - i)$ colour selection or on pre-selected background galaxies to allow ancillary science on photometric redshift confirmations.

In this way, we defined 4574 slits in total for the 25 pointings ranging from 157 to 202 slits per pointing (or 36 to 60 slits per quadrant). Several slits were positioned in such a way to cover more than one target if they had the same declination and a small distance in right ascension. Since the fields are overlapping, about 300 targets have been observed twice and four targets even three times through different masks. This allows us to evaluate the systematic uncertainties of the radial velocity measurements and correct for them between different masks. Discounting all duplications, we ended up with about 4340 unique targets for which spectra were taken.

2.3 Observations

Spectroscopic observations were carried out with the VIable MultiObject Spectrograph (VIMOS, Le Fèvre et al. 2003) in multi-object mode, mounted on the VLT-UT3 Melipal telescope at the

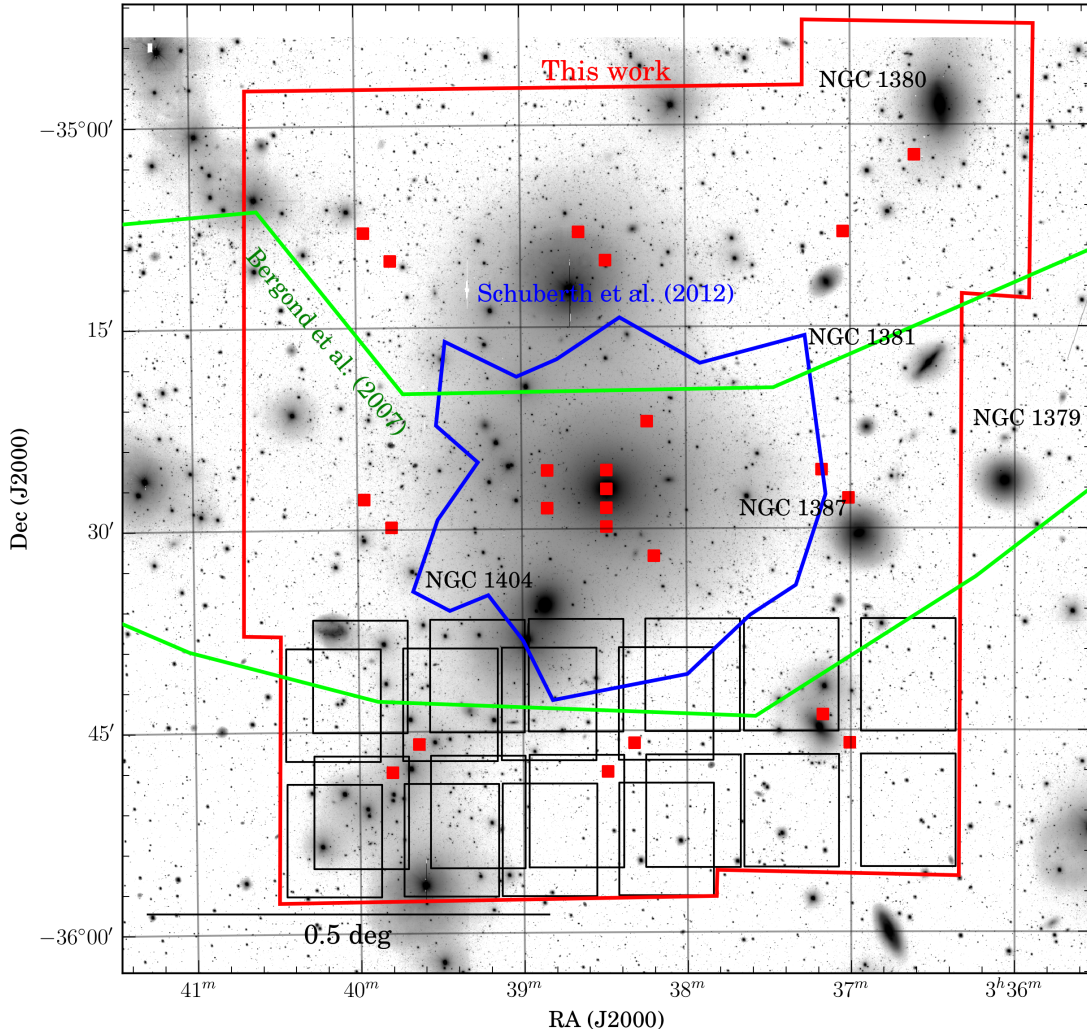


Figure 1. Layout of the observations. The background image is a mosaic of several VST/OmegaCAM pointings in the g -band. The central galaxy is NGC 1399. Additional Fornax galaxies are also labeled. The red boxes mark the centers of all 25 VIMOS pointings. The footprints of some VIMOS masks are shown on the bottom for illustrative purposes. Note how the VIMOS masks are intertwined to maximize spatial coverage. The region covered by all 25 VIMOS is outlined in red, whereas the regions covered by literature studies are shown in green (Bergond et al. 2007) and blue (Schuberth et al. 2010a)

ESO Paranal observatory in Chile. The VIMOS spectrograph was equipped with a filter CG475, which cuts off wavelengths bluer than 4750 \AA , and a MR grating with a spectral resolution $R = 580$ (or 12.0 \AA FWHM) and a dispersion of 2.5 \AA/pix . All slits had a width of 1 arcsec. The pixel scale in the spatial direction was 0.205 arcsec/pix . This setup allows us to explore the spectral window ranging from 4800 to 10000 \AA .

VIMOS is equipped with four CCDs, arranged in four quadrants with chip gaps of ~ 2 arcmin in vertical and horizontal direction (see examples of the VIMOS detector footprints in Figure 1). Overall, one VIMOS mask set covers a field of $4 \times (7 \times 8 \text{ arcmin}^2)$. All masks were observed for 1.5 hours in total, divided into three dithered exposures of 30 minutes. Observations were carried out in service mode in gray-time conditions between October 2014 and January 2015. The seeing ranged from 0.66 arcsec to 1.15 arcsec , with a median of 0.85 arcsec .

2.4 Data reduction

The reduction of the VIMOS data was performed using the Reflex environment (Freudling et al. 2013) of the ESO VIMOS pipeline. For each VIMOS mask, data consist of four quadrants with three individual exposures for each quadrant, flatfields and arc lamp calibration exposures that were taken directly after the science exposures. Each science exposure has a distribution of slits containing the science spectra of the targets contaminated by the emission spectrum of the earth's atmosphere. Since the wavelengths of the sky emission lines are precisely known they can be used for the absolute wavelength calibration of the spectra.

In order to obtain the final wavelength calibrated science spectra, we proceeded as follows. First, a wavelength calibration is performed using the provided arc lamp spectrum. Second, we calculated the residual shift of the sky lines are shifted with respect to their restframe wavelength. For this purpose we provided our own sky line catalog, in which the wavelengths of prominent sky lines, in particular in the Ca triplet region, are listed. The pipeline determines this shift for each spectrum in each science exposure indi-

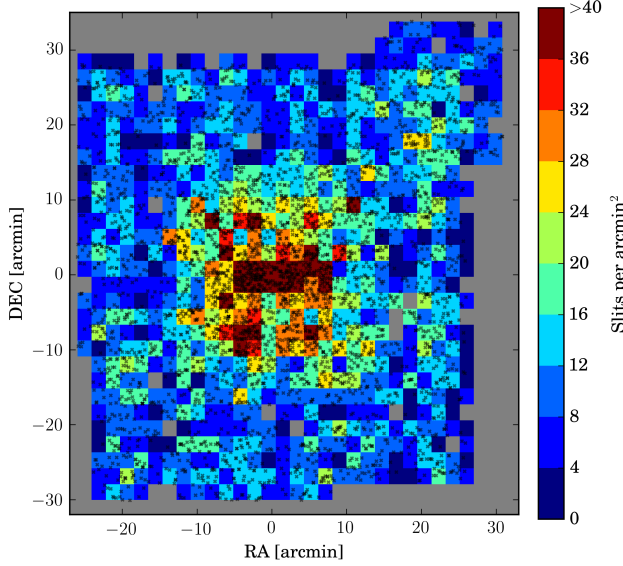


Figure 2. Two dimensional spatial density of VIMOS slits. Slits are shown as small black crosses, whereas the colours represent total counts in boxes of $2 \times 2 \text{ arcmin}^2$. Axes express the distance in arcmin from NGC 1399. More slits were placed towards the center of the cluster, where the target density is higher.

vidually, which is essential because the wavelength shifts are not the same for the three exposures: the shift is largest for the first exposure and smallest for the third exposure. This is caused by the change of instrument flexure between the first science exposure and the final arc lamp exposure. In other words, the third science exposure is taken closest in time, i.e. under almost the same instrument conditions, to the arc lamp exposure, and thus its wavelength calibration is the most accurate one. Finally, the pipeline stacks the three individual science exposures and extracts sky subtracted object spectra from the combined science frame.

Unfortunately, it turned out that the pipeline does not apply the wavelength shifts to the individual spectra before the stacking, meaning that the stacked spectra are not corrected for the residual shifts. This leads to an incorrect absolute wavelength calibration and also to a slight line broadening in the stacked spectra. Even though we cannot correct for the line broadening with the current ESO pipeline version, we found a workaround to correct for the absolute wavelength calibration of the spectra, which is necessary for an accurate measurement of the radial velocities of the objects. To first order, it can be assumed that the median wavelength shift in the stacked spectrum is the same as the one derived for the second exposure. Thus, we re-reduced the second science exposure of all available data to determine the median wavelength shift in each multiplex of each mask by taking the average shift of all spectra in that multiplex. Then, the wavelength of each stacked spectrum was shifted by an amount as determined by the multiplex and the mask in which the spectrum is located. All further analyses were carried out on the corrected spectra.

For each mask, the REFLEX pipeline outputs multi-extension fits files which include the calibrated 2D spectra, the calibrated 1D spectra (and respective errors) and a 2D model of the sky lines. To make the dataset more manageable, we implemented a python/astropy script which copies different data structures corre-

sponding to each slit into a multi-extension fits file. Each slit is associated to a fits file which contains: the 1D scientific spectrum, the 1D error spectrum, the sky-subtracted, wavelength-corrected 2D spectrum and a thumbnail of the object of $5 \times 5 \text{ arcsec}^2$ from *g*-band VST imaging.

3 REDSHIFT ESTIMATION

A total of 6700 spectra were extracted by the REFLEX pipeline. This number includes the genuine physical objects associated with the Fornax cluster (i.e., GCs, UDCs or dwarf galaxies), as well as Galactic stars, background galaxies and sources with signal-to-noise (S/N) too low to be classified with certainty.

Radial velocities were computed with iraf/fxcor, which performs cross-correlation between the Fourier-transformed scientific spectrum and a Fourier-transformed set of template spectra (Tonry & Davis 1979). Fxcor was preferred to full spectra fitting approaches (e.g. pPXF, Cappellari & Emsellem 2004) because the former does not require initial guesses on the radial velocity and it is more CPU efficient.

The Indo-U.S. Library of Coudé Feed Stellar Spectra (Valdes et al. 2004) was used as library of template spectra. The library contains 1273 stellar spectra, observed with a dispersion of 0.44 \AA/pix and a resolution of $\sim 1 \text{ \AA}$. The spectra cover the $3460 - 9464 \text{ \AA}$ range, which overlaps nicely with the wavelength range of our VIMOS spectra. From the whole library, we selected a random subset of 40 stars with spectral types from *F* to *M* because this is the range expected for metal-poor to metal-rich GCs. The 40 stellar spectra were convolved with a Gaussian filter of standard deviation $\sigma = 12.0 \text{ \AA} / 2.355$ (where 12.0 \AA is the FWHM resolution of our VIMOS spectra).

The scientific spectra were prepared as follows. First, we computed the median signal-to-noise per pixel S/N , where the signal S is measured in the range $5000-6600 \text{ \AA}$ and the noise N is the noise returned by the REFLEX pipeline in the same wavelength range. Second, telluric bands in the range $6850 - 7688 \text{ \AA}$ and some troublesome skylines were replaced with the fit to the spectral continuum. The continuum was computed with iraf/continuum by averaging ten contiguous pixels and interpolating the result with a cubic spline coupled with a 3σ rejection algorithm.

Naively, one may think that cross-convolving the full wavelength range of our VIMOS spectra will return more robust radial velocities because the number of atomic lines used for the convolution is larger. Instead, we tested that using the whole wavelength range can increase uncertainties due to severe template mismatches, likely due to the low ($S/N = 12$) average S/N of our spectra. Therefore, we chose to run fxcor on the region surrounding the Calcium Triplet (CaT) at $8498-8548-8662 \text{ \AA}$, because these three lines occupy a very narrow wavelength range. Therefore, we correlate the scientific spectra between $8485-8750 \text{ \AA}$ with the template spectra between $8450-8720 \text{ \AA}$. This means that we are able to measure the radial velocities of unresolved objects between -500 km s^{-1} and $+3000 \text{ km s}^{-1}$, which include both Galactic stars and Fornax objects.

During the fxcor run, and prior to the correlation with the template spectra, the Fourier-transformed scientific spectra were filtered with a ramp filter. The filter was setup to cut-off noisy high frequencies as well as low frequencies which may result from poor continuum fitting. The continuum was fitted with a cubic spline function. We ran fxcor in non-interactive mode, meaning that fxcor always returns the velocity corresponding to the highest cross-

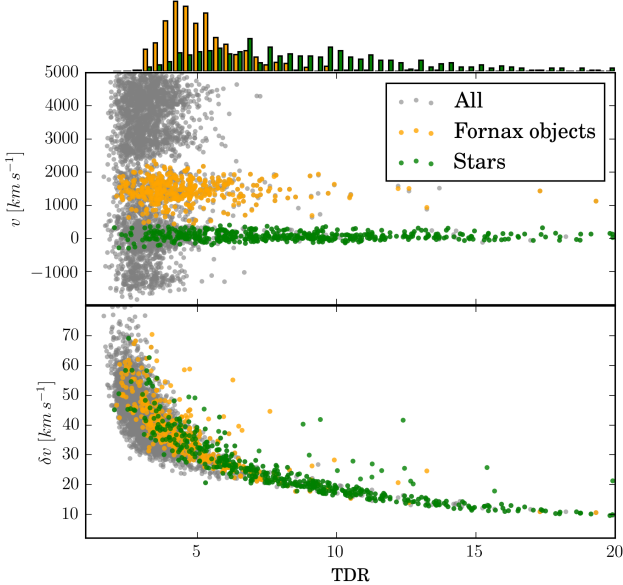


Figure 3. Results from iraf/fxcor for ~ 4200 spectra. The x-axis represents the Tonry & Davies R parameter (TDR) which is a proxy for the goodness of the cross-correlation between the scientific and the template spectra. Smaller TDR corresponds to larger velocity uncertainties δv (bottom panel) and therefore to a poorer spectral fit. The measured radial velocity v is shown on the y-axis of the top panel. The sequence of objects at $v \approx 0 \text{ km s}^{-1}$ are Galactic stars, whereas the cluster at $v \approx 1700 \text{ km s}^{-1}$ are GC candidates in the Fornax cluster. The histogram on the top shows raw counts for stars and Fornax objects only, respectively.

correlation with the template spectrum. The final radial velocity is the median of the single radial velocities obtained from the cross-correlation with the 40 template stars. To overcome extreme template mismatch (i.e. the case in which the fitted radial velocity varies considerably depending on the adopted template), we used a median-absolute-deviation algorithm (MAD) to flag radial velocities deviating more than 5σ from the median of the radial velocities obtained from the 40 template stars. Outliers, if any, are removed from the velocity set and the final radial velocity and error are computed from the remaining measurements. 90 per cent of GCs and stars have between 0 to 5 outliers, suggesting that the effect of extreme template mismatch is small.

The scatter in radial velocity due to normal template mismatch (i.e. due to intrinsic mixture of stellar populations in GCs) varies between $3 - 10 \text{ km s}^{-1}$ (after removing outliers) depending on the S/N of the spectrum. The final error on the radial velocity is the median velocity error returned by fxcor summed in quadrature to the scatter due to normal template mismatch.

We used the Tonry & Davis (1979) R factor (TDR hereafter) to assess the goodness of the correlation between scientific spectra and template spectra. As expected, TDR is inversely proportional to the velocity uncertainties. This effect is shown in Figure 3, where TDR is shown as a function of the measured radial velocity v and velocity uncertainty δv . It is worth noting that fxcor was set to measure the Doppler shift of the CaT lines only for objects with radial velocities $-500 < v < 3000 \text{ km s}^{-1}$. This means that only radial velocities measured to be $-450 < v < 2500 \text{ km s}^{-1}$ are meaningful, whereas velocities outside this range are non-physical, and

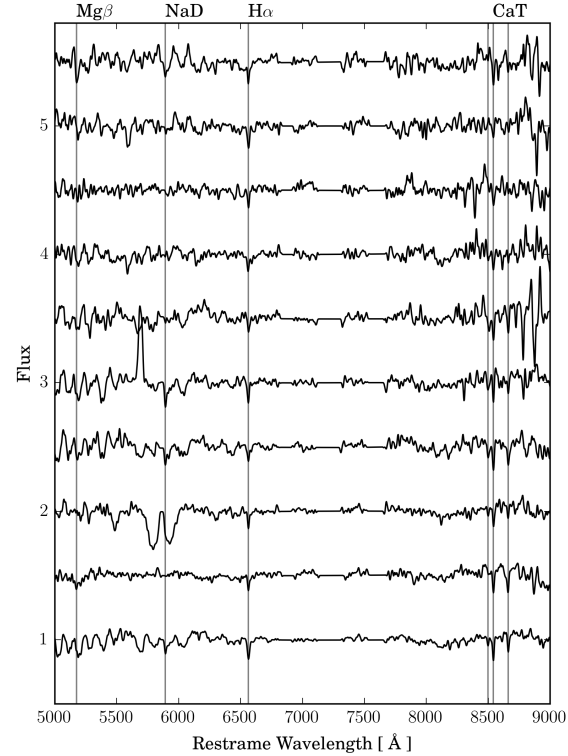


Figure 4. A sample of GC spectra suitably normalised. Shown are continuum-normalized redshift-corrected spectra for GCs with increasing S/N (from top to the bottom). The spectrum at the top has $S/N = 15$, the one at the bottom $S/N = 50$. The main atomic lines are labelled on the top. Features such as the strong absorption in the spectrum at Flux = 2 and the emission in the spectrum at Flux = 3 are instrumental artifacts and not physical features of the GC. The flat horizontal lines between 7000-8000 \AA mark regions with masked skylines (see text)

thus meaningless. Heliocentric correction was applied to all radial velocities.

3.1 Disentangling Fornax objects from foreground and background contamination

We are interested in separating objects physically bound to the Fornax cluster (GCs, UCDs and galaxies) from objects unrelated to the Fornax cluster (Galactic stars and foreground or background galaxies). A first distinction can be performed on the basis of the systemic velocity. We use the same velocity range adopted by Schuberth et al. (2010a) for GCs and Galactic stars. Using the top panel of Figure 3 as a reference, Fornax objects are those with $450 \leq v < 2500 \text{ km s}^{-1}$ (850 datapoints), whereas Galactic stars are those with $-450 < v < 450 \text{ km s}^{-1}$ (956 datapoints). The velocity determination of background galaxies and their distribution will be discussed in a separate paper.

Spectra of Fornax objects (GCs, UCDs) and Galactic star candidates were redshift-corrected and eyeballed. We checked for the correct positions of the following lines: CaT, H α (6563 \AA), NaD(5892 \AA), Mg β (~5175 \AA) and H β (~4861 \AA). The CaT and H α lines, if present, are always visible, whereas the Mg β line is hardly recognizable in spectra with $S/N \lesssim 10$. The NaD is not

always visible because this atomic line is shifted onto a problematic skyline at 5860–5890 Å for spectra with $v \lesssim 1000 \text{ km s}^{-1}$. The H β line, at which the instrumental efficiency is less than 20 per cent, can be discerned only for spectra with $S/N \gtrsim 20$.

Figure 4 showcases some spectra with S/N ranging from 50 (bottom spectrum) to 15 (top spectrum). The GG475-filters of the first and third quadrant, coupled with the MR-grism, introduce an absorption feature between about $5600 < \lambda < 6300 \text{ \AA}$ (see the third spectrum from the bottom in Figure 4 for an example). This occurs because the GG475-filter is composed of 10–20% in its weight by sodium oxide. Impure manufacturing likely caused this feature; however, it does not affect our analysis because the blue part of the spectra is not used for our velocity measurements. Strong emission features can occasionally appear in the blue part of the spectra (see the fifth spectrum from the bottom in Figure 4), but they are attributed to zero order overlaps that are not corrected for by the Reflex reduction pipeline, rather than to physical phenomena associated to the light source.

For spectra with very low S/N the distinction between atomic lines and noise features becomes somewhat subjective. Therefore, all 850 Fornax object candidates were independently eyeballed by five members of the team. The inspection was performed on a dashboard including the 2D image of the source, the redshift corrected spectrum and attributes such as magnitude and S/N. We gave a vote of 1 to spectra which were certainly Fornax objects and 0 to non-Fornax object spectra. We found that 323 spectra received a vote of 5/5 (meaning that these spectra were classified as Fornax objects by all members of the team), 348 spectra received a vote of 4/5 and 420 spectra received a vote of 3/5. In the followings, we will use the last set of 420 spectra as our final spectroscopic catalogue of the Fornax cluster.

We repeated the above procedure to select a sample of spectroscopically confirmed Galactic stars with radial velocities in the range $-450 < v < +450 \text{ km s}^{-1}$, finding a total of 492 Galactic stars.

4 RESULTS

4.1 Velocity self-consistency

We measured radial velocities for 51 duplicated objects (including Galactic stars), observed across multiple VIMOS masks. The velocity difference Δv between duplicated objects is shown in Figure 5 as a function of g magnitude. We detected no clear trend between Δv and the magnitude. One object has a velocity difference which scatters more than 3σ from the average. We attributed this disagreement to an issue with the wavelength calibration for this particular object. The root-mean-square of the velocity difference (of GCs and stars combined) is 91 km s^{-1} , which becomes 79 km s^{-1} after clipping the outlier.

We averaged the radial velocities of the duplicated GCs and summed in quadrature their velocity uncertainties. This left us with a catalogue of 387 Fornax objects and 464 Galactic stars.

4.2 Comparison with literature data

The stellar systems surrounding NGC 1399 has been in the focus of many spectroscopic studies (Dirsch et al. 2004; Schuberth et al. 2010b; Bergond et al. 2007; Firth et al. 2007; Chilingarian et al. 2011; Mieske et al. 2004; Hilker et al. 2007; Francis et al. 2012; Drinkwater et al. 2000).

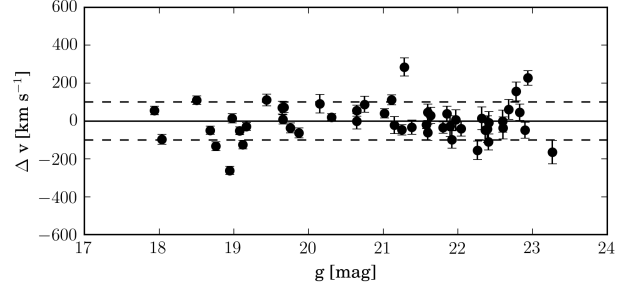


Figure 5. Internal velocity comparison. The figure shows the velocity difference Δv between GCs with two independent velocity measurements. The full and dashed line represent $\delta v = 0 \text{ km s}^{-1}$ and $\delta v = \pm 100 \text{ km s}^{-1}$, respectively.

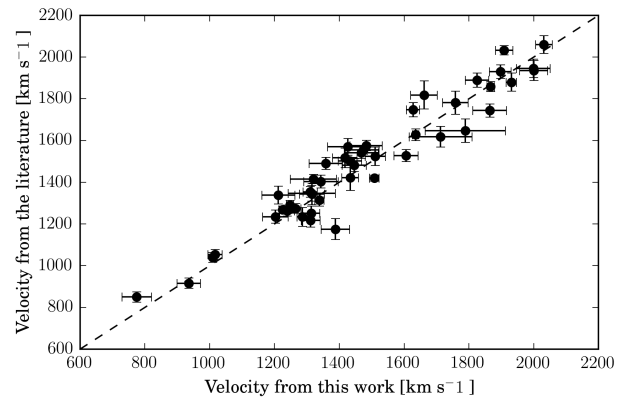


Figure 6. Comparison with literature studies. The radial velocity of literature objects is averaged among literature studies as discussed in the text. The 1 to 1 line is shown as dashed line.

To find which of our VIMOS objects have a literature counterpart, we matched our catalogue of 387 Fornax objects with the NED (Nasa/Ipac Extragalactic Database) database using the python/astropy tools. We manually added the catalogue of Schuberth et al. (2010a) to the literature database, because the 693 GCs from Schuberth et al. (2010a) are not in NED. We required the literature objects to have a measured radial velocity and to be within 0.4 arcsec from our VIMOS source.

In most cases, the literature counterpart has been observed by more than one author. Table 1 reports the number of objects per author for which we have a VIMOS radial velocity. In order to compare literature velocities with our VIMOS velocities, we averaged together the radial velocities of unique objects observed in multiple literature studies. Uncertainties were summed in quadrature. Overall, we found 48 of our Fornax objects to have a literature counterpart.

Figure 6 shows the comparison between our VIMOS objects and the unique literature objects obtained as explained above. Also in this case the agreement is satisfactory and no bias is detected.

4.3 Classification of Fornax objects

We classified all Fornax objects based on their morphology: namely GCs, ultra compact dwarfs (UCDs) and background galaxies. The

Paper	Number of duplicated objects
Dirsch et al. (2004)	29
Schuberth et al. (2010b)	26
Bergond et al. (2007)	14
Firth et al. (2007)	11
Chilingarian et al. (2011)	2
Mieske et al. (2004)	1
Hilker et al. (2007)	1
Francis et al. (2012)	1
Drinkwater et al. (2000)	1

Table 1. Number of confirmed VIMOS objects also found in archival data (grouped by author).

spatial resolution of VST/OmegaCam is insufficient to resolve the typical half-light radii of GCs with $r_h < 10\text{pc}$ (Masters et al. 2010; ?). Although the size of UCDs with $r_h > 20\text{ pc}$ can be resolved using our imaging data (Cantiello et al. 2015), measuring UCD sizes is not the focus of this paper and will be deferred to a future work.

It is established that a sharp magnitude cut cannot perfectly separate UCDs from GCs. However, it has been shown (Voggel et al. 2016; Eigenthaler et al. 2018) that the bulk of UCDs with confirmed sizes in the Fornax cluster have $M_V \leq 10$ ($\approx M_i \leq 11$). Therefore, we use this magnitude cut as benchmark value to separate UCDs with $i \leq 20.3$ from GCs with $i > 20.3$. This selection returns 15 UCDs and 372 GCs.

The object at $\alpha = 3:36:37.253$ $\delta = -35:23:09.20$ is the nucleus of the nucleated dwarf galaxy FCC 171, whose radial velocity was first measured in Bergond et al. (2007). This object will be treated as GCs in the following analysis.

5 DISCUSSION

In this section we discuss some qualitative properties of the final dataset. We look at the spatial distribution and phase-space diagrams. A detailed kinematic and dynamic analysis (rotation curve, dark matter modelling, luminosity function analysis) will be subject of forthcoming papers.

5.1 Phase-space and spatial distribution

The phase-space diagram and the spatial distribution are shown in Figure 7. In both cases, GCs, UCDs and Galactic stars are compared to the catalogues of Bergond et al. (2007) and Schuberth et al. (2010a). These two catalogues are the largest and most homogeneous in the literature. Moreover, the catalogue of Schuberth is an extension of the catalogue of Dirsch et al. (2004). Together they include sources within 18 arcmin from NGC 1399. Bergond's catalogue was designed to target intra-cluster globular clusters and it is more radially extended (see also Figure 1). It covers a strip of about 1.5 degree in right ascension and half a degree in declination. The catalogues of Schuberth and Bergond combined provide a good representation of the current archival phase-space and spatial distribution of the GC system in the core of the Fornax cluster.

The left figure shows that the velocity distribution of GCs/UCDs is well separated from that of Galactic stars, although a few GCs between $10 < R < 20$ arcmin might be misclassified Galactic stars. It is also clear that the velocity distribution of GCs is skewed towards bluer velocities, an effect already noticed in (Schuberth et al. 2010a).

The systemic velocity of GCs and UCDs is $v_{\text{GCs}} = 1443 \pm 18\text{ km s}^{-1}$ and $v_{\text{UCDs}} = 1413 \pm 91\text{ km s}^{-1}$, respectively. These are both consistent with the average systemic velocity from the literature $v_{\text{NED}} = 1425 \pm 4\text{ km s}^{-1}$. Our sample also includes interlopers from large galaxies surrounding NGC 1399, in particular NGC 1380, NGC 1404, NGC 1387. The position of these three galaxies in the phase-space diagram is marked with a red cross.

It is not trivial to disentangle the GC population of NGC 1380 and NGC 1404 because of their proximity in phase-space to NGC 1399. Here we adopt a conservative approach to extract the GC system of these galaxies, but we acknowledge that more complex methodologies can return more accurate results. Following Schuberth et al. (2010a), we use 3 arcmin from the galaxy centre as a benchmark radius to select the bulk of GCs associated with these galaxies. We also require that the radial velocity of the GCs should be within $v_{\text{sys}} \pm 2\sigma$ the systemic velocity of the host galaxy, where σ is the galaxy stellar velocity dispersion. Here we used $\sigma = 247\text{ km s}^{-1}$ (Vanderbeke et al. 2011), $v_{\text{sys}} = 1947\text{ km s}^{-1}$ for NGC 1404 and $\sigma = 170\text{ km s}^{-1}$ (Wegener et al. 2003), $v_{\text{sys}} = 1302\text{ km s}^{-1}$ for NGC 1387, respectively. After applying the above selection criteria, we found 17 and 8 GCs associated with NGC 1404 and NGC 1387, respectively. The larger number of GCs associated to NGC 1404 is a due to the galaxy being more massive than NGC 1387, but also to its proximity to NGC 1399 which increases the fraction of contaminants. In case of NGC 1380, with $\sigma = 190\text{ km s}^{-1}$ (Vanderbeke et al. 2011) and $v_{\text{sys}} = 1877\text{ km s}^{-1}$, the identification of its GC system is easier given its isolated position. Using the criteria above, we found 7 GCs associated with this galaxy.

The right panel of Figure 7 displays the spatial distribution of our GC and UCD catalogues. This diagram also shows how our catalogue is complementary to literature catalogues: it increases the object sampling in the central regions of the galaxy and it fills gaps with no data in the outer regions.

GC systems which are bond to other giant galaxies can be seen clustered around their centres. Figure 7 suggests that our combined sample might also contain some GCs belonging to NGC 1379 and NGC 1381 (see Figure 1).

5.2 Photometric diagrams

Figure 8 displays the distribution of GCs/UCDs in the photometric space. These are compared with the distribution of all sources targeted for spectroscopic follow-up, including Galactic stars and background galaxies. Although the u filter is known to well discriminate GCs from contaminants, here we only consider g, r, i magnitudes because all but one GCs/UCDs have a genuine measurement in these photometric bands, whereas only 50% of our GCs/UCDs have a u -band measurement. This is due to u -band imaging being shallower than the other bands for detecting faint GCs (D'Abrusco et al. 2016).

GCs/UCDs and contaminants are not well separated using merely g, r, i filters, but velocity information clearly separates GCs/UCDs from Galactic stars and background galaxies. This is also shown in Figure 8. The left-bottom panel, with $(g-i)$ vs $.v$, shows how the velocity dispersion of blue GCs with $(g-i) \leq 1$ is higher than that of the red GCs, a property shared with GC systems in the most giant galaxies. The rightmost panel, with v vs i , shows that the velocity distribution of all GCs is skewed towards lower velocities (a property also visible in Figure 7). The convincing separation between GCs and stars also ensures that this property is unlikely due miss-classified to GCs.

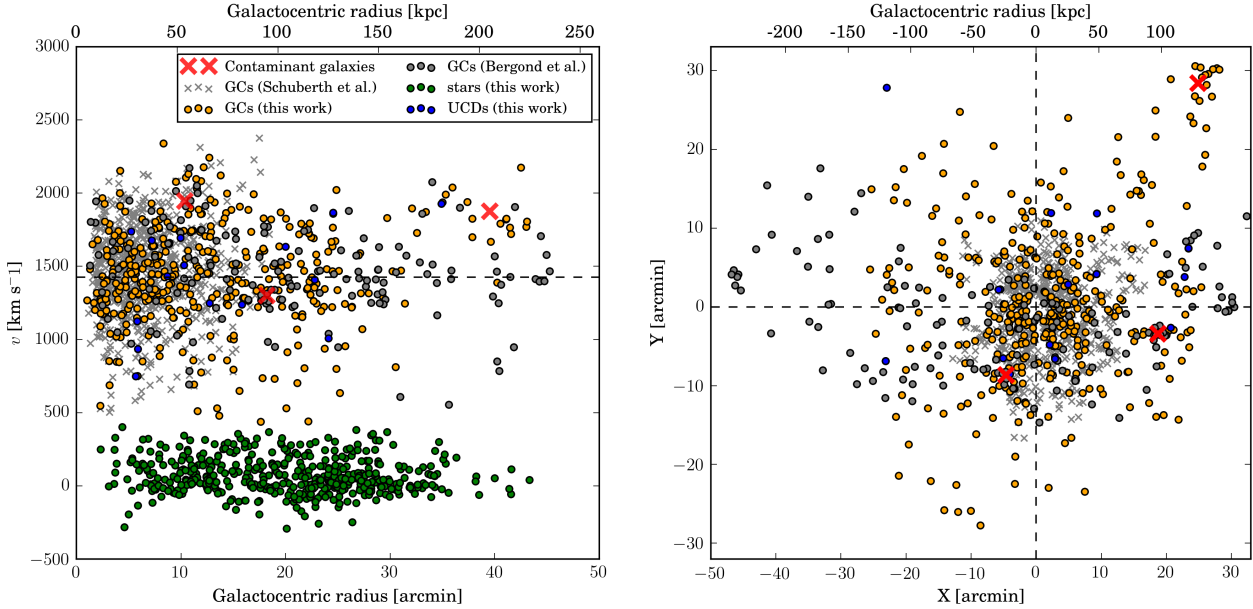


Figure 7. *Left:* Phase-space velocity diagram. The figure shows the measured systemic velocity of the Fornax objects presented in this paper (orange points), GCs from Schuberth et al. (2010a) (grey crosses), GCs from Bergond et al. (2007) (grey points) and Galactic stars measured in this paper (green points). The systemic velocity of NGC 1399 is marked with a dashed line at $v = 1425 \text{ km s}^{-1}$. The systemic velocity and galactocentric distance of giant Fornax galaxies (namely NGC 1404, NGC 1387, NGC 1380) are shown as red crosses. Physical distances in kpc are also shown on the top panel. *Right:* Position diagram. The plot shows the spatial distribution of the objects from the left panel (except for Galactic stars for clarity). The distance is expressed in arcminutes from the centre of NGC 1399. Physical distances in kpc are also shown on the top panel. Note how the GCs from our paper complement the GC catalogues of Schuberth et al. (2010a) and (Bergond et al. 2007).

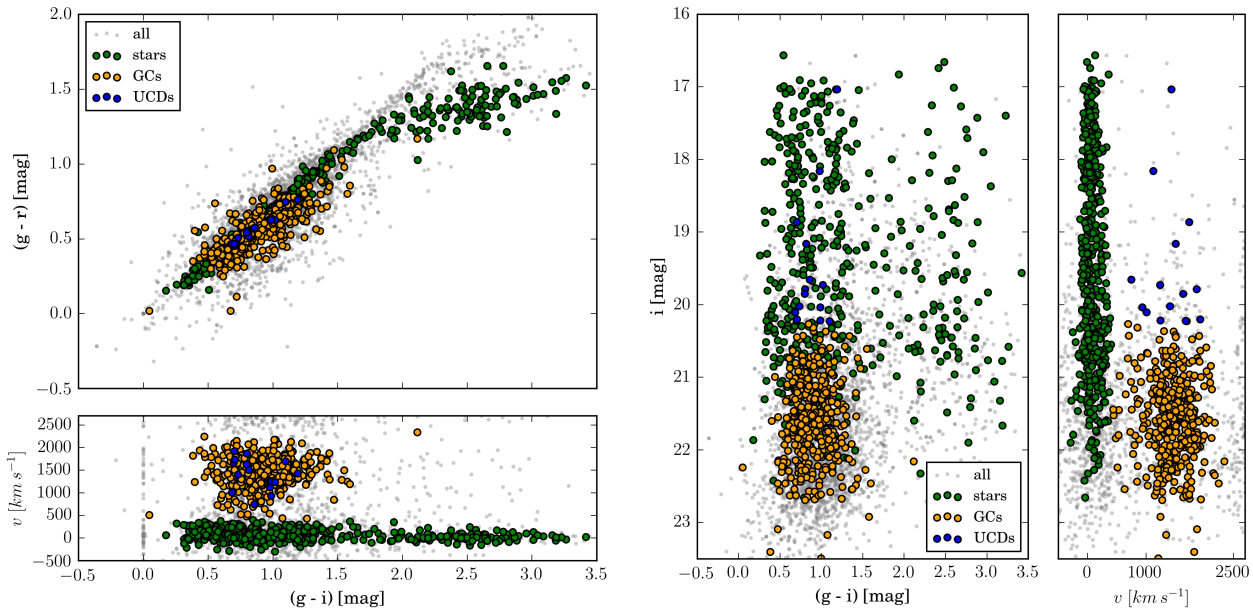


Figure 8. Colour-colour and colour-magnitude diagram. The figure shows the distribution of the labelled objects in a $(g - i)$ vs. $(g - r)$ space (left panel) and $(g - i)$ vs i space (right panel). Each diagram includes also a radial velocity v axis to show the separation of GCs/UCDs from stars and galaxies. The objects labelled as ‘all’ represent all sources targeted for spectroscopic follow-up and not the photometric master catalogue.

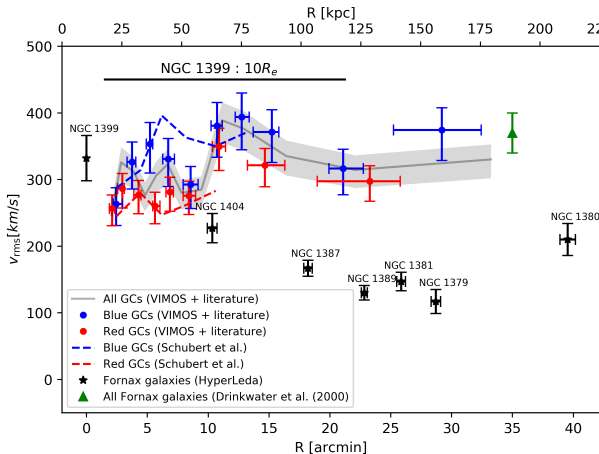


Figure 9. Root-mean-square velocity dispersion of NGC 1399 stellar system. The blue and red points represent the blue and red GCs/UCDs, respectively, whereas the full grey-line shows the full master catalogue of 1133 stellar objects. Bins are of irregular size, reflected in the asymmetric radial error bars representing the 25-th and 75-th quantiles. The digitised v_{rms} profiles from Schuberth et al. (2010a) are the blue and red dashed lines, without uncertainties for clarity. The central stellar velocity dispersion for the galaxies in the field are the black points, with the error bars on the x-axis representing one effective radius.

5.3 Root-mean-square velocity profile

The root-mean-square velocity v_{rms} quantifies the total kinetic energy of a stellar system. It accounts both for the ordered and for the random stellar motions. Here we compute the root-mean-square velocity as:

$$v_{\text{rms}}^2 = \frac{1}{N} \sum (v_i - v_{\text{sys}})^2 - (\Delta v_i)^2. \quad (1)$$

where v_i is the radial velocity of the i-th GC and Δv_i is its uncertainty. $v_{\text{sys}} = 1425 \text{ km s}^{-1}$ is the systemic velocity of NGC 1399. Uncertainties were derived with the formulae provided by Danese et al. (1980).

The v_{rms} was calculated on a total of 1133 stellar objects. This catalogue is made of the 387 objects discussed in this paper, combined with the catalogues of Bergond et al. (2007) and Schuberth et al. (2010a). If an object was found in more than one catalogue we computed its average radial velocity with the uncertainties summed in quadrature. Also, GCs and UCDs from literature catalogues were given the VST photometry discussed in this work. Therefore, no photometric calibration was required. The v_{rms} profile was computed in radial bins. Bins were of irregular size. However, each bin contained roughly the same number of objects, namely : 48, 66, 88 objects per bin for the blue, red and all GCs/UCDs, respectively.

Figure 9 displays the v_{rms} profile for: i) our combined master catalogue of 1133 GCs and UCDs; ii) the GC catalogue of (Schuberth et al. 2010a), iii) the central stars of galaxies surrounding NGC 1399; iv) all Fornax galaxies from Drinkwater et al. (2000).

The master catalogue contains GCs and UCDs predominantly from NGC 1399, which is the largest and more massive system in the field dominating the total potential in the core of the cluster. Here, objects from other galaxies, embedded in the extended exponential halo around the galaxy (Iodice et al. 2016), in particular NGC 1404, NGC 1387, are likely to contaminate the kinematics of the central galaxies. However, looking at the v_{rms} profile of the total sample (shaded gray area) there is a steep rise of the profile

around $R \sim 10$ arcmin which marks a kinematical transition from a “colder” kinematical region to a “warmer” one. In the outermost region, the v_{rms} profile flattens out to a value which is fairly consistent with the kinematics of the cluster galaxies (the green data point at $R \sim 35$ from Drinkwater et al. 2000). This suggests that the GC kinematics at radii larger than 10 arcmin is ruled by the cluster potential. This feature, kinematically demonstrates that the transition radius between the bright central galaxy and the outer exponential halo at $R \sim 10$ arcmin from Iodice et al. (2016) represents the radius where we observe the emergence of an intracluster population of GCs. A similar conclusion is found from the new observations of PNe from Spinelli et al. (2018), hence all evidences converging, for the first time, on a clear photometrical and kinematical evidence of the intracluster light in the Fornax Cluster.

When split in the red and blue subpopulations the GC sample shows some systematic differences. At all radii the v_{rms} profile of the red GCs is systematically smaller than the one of the blue GCs. In the innermost regions at $R < 10$ arcmin they are consistent with the results from Schuberth et al. (2010a). In particular the blue GCs turned out to be the more extended population in radius, nicely matching the value of the cluster galaxy datapoint. The difference in normalisation between the two populations is mainly deriving from the different slopes of the two populations density profiles as measured, e.g., by Schuberth et al. (2010a, their Eq. 10 and 11 and Table 5). However, the difference of the measured slopes are so small that using Eq. 2 to 4 in Napolitano et al. (2014) to determine the expected change in the normalisation of the two profiles, we have found that for a $\sigma \sim 300 \text{ km s}^{-1}$ of the RGC value the estimated BGC value of v_{rms} is $\sim 308 \text{ km s}^{-1}$, i.e. consistent with what measured for the Blue GC datapoint.

Finally, we report in the same Figure the central velocity dispersion values of the galaxies populating the same area occupied by the total GC catalog. The central value of NGC 1399 is consistent with the typical central rise of the velocity dispersion in the center of massive galaxies where is the potential on the galaxy which dominates. At larger distances one might expect that galaxy might contaminate to the overall GC kinematics. Especially in the outer regions, i.e. $R > 10$ arcmin, assuming these regions dominated by the cluster potential, the presence of GCs bound to the galaxies might alter the true intracluster population. A detailed separation of the bound GC population from the true unbound (from any galaxy in the core) GCs will be addressed in a forthcoming paper. Here we just remark that the impact of the bound GC population has to be limited because, roughly speaking, it should dilute the true dispersion by a quantity that it is roughly the difference in quadrature of the true dispersion and the one of the bound sample (i.e. assuming the central velocity dispersion of the galaxy). If so, then the dilution can be as large as 10-15%, which is enough to explain the saddle in the v_{rms} profile in the radius range $15 < R < 28$ arcmin corresponding to the bins overlapping with NGC 1387, NGC 1389, NGC 1381 and NGC 1379, while a similar correction for NGC 1404 would increase the intrinsic v_{rms} to $\sim 400 \text{ km s}^{-1}$.

In conclusion of this section, we can summarise the main finding of this paper in Figure 9, by saying that the unprecedented extension of the GC kinematics, combined with the literature data, has demonstrated the kinematical signature of a population of intracluster GCs, made of both Red GCs and Blue GCs. The two populations show v_{rms} profiles consistent with the dynamics of a common cluster potential and also consistent with the velocity dispersion of the innermost cluster galaxies in the Fornax cluster.

Analogous signatures of intracluster stellar populations have been shown previously in the Virgo and Fornax clusters (see e.g.,

Arnaboldi et al. 2004; Longobardi et al. 2015; Paolillo et al. 2002) but the catalog presented here will offer a unique chance to perform a fully dynamical analysis of both the bound and unbound GC populations (D'Abrusco et al. 2016).

6 CONCLUSIONS

In this paper, we presented the results of a large spectroscopic survey of GCs in the Fornax cluster, focusing on observations, data reduction and compilation of the final catalogue. The survey is part of the ongoing Fornax Deep Survey, which aims to study the formation, evolution and dynamics of galaxies and small stellar systems in the Fornax cluster and of its members.

Our results are based on observations with VST/OmegaCam for imaging and 25 VST/VIMOS masks for spectroscopic follow-up. Objects were pre-selected in multi-band imaging, supported also by the many spectroscopic catalogues already present for this region of the sky. Approximately 4500 objects were observed. The total observation time was 37.5 hours, mostly in sub-arcsec seeing conditions. Data reduction was performed using the ESO VIMOS pipeline. Redshifts were extracted using iraf/fxcor, whereas the remaining data analysis was carried out using the python suite. Only the Calcium Triplet region was used for redshift estimation, but the quality of the fit was assessed using the full spectrum from 4800 to 10000 Å.

After a visual inspection of candidate spectra, we compiled a consensus catalogue of 372 GCs, 15 UCDs (objects with $i \leq 20.3$ mag) and 464 Galactic stars. Most GCs belong to the dominant galaxy NGC 1399, but we estimated that 30–40 objects might belong to NGC 1404, NGC 1380, and to other major galaxies in the observed field.

We have used the new complete catalog of GCs to derive the total v_{rms} of the GC sample and also broken the sample in the Red and Blue subsamples. We have demonstrated that all profiles show a similar signature at around $R \sim 10$ of a kinematical transition from a low v_{rms} regime to a higher one, with the former being consistent with the central velocity dispersion of NGC 1399 (the central cluster galaxy) and the latter being consistent with the velocity dispersion of the cluster galaxies. This demonstrates that at $R > 10$ the GC populations both feel strongly the cluster potential, rather than the fable galaxy potential. These kinematical evidences corroborate the photometrical evidences found in the deep galaxy photometry of a transition radius between the bright central galaxy and the outer exponential halo at $R \sim 10$ arcmin from Iodice et al. (2016) and show, from the dynamical point of view, the emergence of an intracluster population of GCs in the Fornax Cluster.

REFERENCES

- Arnaboldi M., Gerhard O., Aguerri J. A. L., Freeman K. C., Napolitano N. R., Okamura S., Yasuda N., 2004, ApJ, 614, L33
 Bassino L. P., Richtler T., Dirsch B., 2006, MNRAS, 367, 156
 Bergond G., Athanassoula E., Leon S., Balkowski C., Cayatte V., Chemin L., Guzmán R., Meylan G., Prugniel P., 2007, A&A, 464, L21
 Cantiello M., Capaccioli M., Napolitano N., Grado A., Limatola L., Paolillo M., Iodice E., Romanowsky A. J., Forbes D. A., Raimondo G., Spavone M., La Barbera F., Puzia T. H., Schipani P., 2015, A&A, 576, A14
 Cappellari M., Emsellem E., 2004, PASP, 116, 138
 Chilingarian I. V., Mieske S., Hilker M., Infante L., 2011, MNRAS, 412, 1627
 D'Abrusco R., Cantiello M., Paolillo M., Pota V., Napolitano N. R., Limatola L., Spavone 2016, ApJ, 819, L31
 Danese L., de Zotti G., di Tullio G., 1980, A&A, 82, 322
 Dirsch B., Richtler T., Geisler D., Gebhardt K., Hilker M., Alonso M. V., Forte J. C., Grebel E. K., Infante L., Larsen S., Minniti D., Rejkuba M., 2004, AJ, 127, 2114
 Drinkwater M. J., Phillipps S., Jones J. B., Gregg M. D., Deady J. H., Davies J. I., Parker Q. A., Sadler E. M., Smith R. M., 2000, A&A, 355, 900
 Eigenthaler P., Puzia T. H., Taylor M. A., Ordenes-Briceño Y., Muñoz R. P., Ribbeck K. X. a., 2018, ArXiv e-prints
 Firth P., Drinkwater M. J., Evstigneева E. A., Gregg M. D., Karick A. M., Jones J. B., Phillipps S., 2007, MNRAS, 382, 1342
 Francis K. J., Drinkwater M. J., Chilingarian I. V., Bolt A. M., Firth P., 2012, MNRAS, 425, 325
 Freudling W., Romaniello M., Bramich D. M., Ballester P., Forchi V., García-Dabló C. E., Moehler S., Neeser M. J., 2013, A&A, 559, A96
 Hilker M., Baumgardt H., Infante L., Drinkwater M., Evstigneeva E., Gregg M., 2007, A&A, 463, 119
 Iodice E., Capaccioli M., Grado A., Limatola L., Spavone M., Napolitano N. R., Paolillo M., Peletier R. F., Cantiello M., Lisker T., Wittmann C., Venhola A., Hilker M., D'Abrusco R., Pota V., Schipani P., 2016, ApJ, 820, 42
 Le Fèvre O., Saisse M., Mancini D., Brau-Nogue S., Caputi O., Castinel L., D'Odorico S., Garilli B., Kissler-Patig M., Lucuix C., Mancini G., Pauget A., Sciarretta G., Scodéggi M., Tresse L., Vettolani G., 2003, in Iye M., Moorwood A. F. M., eds, Instrument Design and Performance for Optical/Infrared Ground-based Telescopes Vol. 4841 of Proc. SPIE, Commissioning and performances of the VLT-VIMOS instrument. pp 1670–1681
 Longobardi A., Arnaboldi M., Gerhard O., Hanuschik R., 2015, A&A, 579, A135
 Masters K. L., Jordán A., Côté P., Ferrarese L., Blakeslee J. P., Infante L., Peng E. W., Mei S., West M. J., 2010, ApJ, 715, 1419
 Mieske S., Hilker M., Infante L., 2004, A&A, 418, 445
 Muñoz R. P., Puzia T. H., Lançon A., Peng E. W., Côté P., Ferrarese 2014, ApJS, 210, 4
 Paolillo M., Fabbiano G., Peres G., Kim D.-W., 2002, ApJ, 565, 883
 Puzia T. H., Paolillo M., Goudfrooij P., Maccarone T. J., Fabbiano G., Angelini L., 2014, ApJ, 786, 78
 Schuberth Y., Richtler T., Hilker M., Dirsch B., Bassino L. P., Romanowsky A. J., Infante L., 2010a, A&A, 513, A52
 Schuberth Y., Richtler T., Hilker M., Dirsch B., Bassino L. P., Romanowsky A. J., Infante L., 2010b, A&A, 513, A52
 Tonry J., Davis M., 1979, AJ, 84, 1511
 Valdes F., Gupta R., Rose J. A., Singh H. P., Bell D. J., 2004, ApJS, 152, 251
 Vanderbeke J., Baes M., Romanowsky A. J., Schmidtobreick L., 2011, MNRAS, 412, 2017
 Voggel K., Hilker M., Richtler T., 2016, A&A, 586, A102
 Wegner G., Bernardi M., Willmer C. N. A., da Costa L. N., Alonso M. V., Pellegrini P. S., Maia M. A. G., Chaves O. L., Rité C., 2003, AJ, 126, 2268